# Characterization of Additively Manufactured Suspended Finite Ground CPW Interconnects Enhanced by Femtosecond Laser Micromachining

Omer Faruk Firat<sup>®</sup>, Student Member, IEEE, Jing Wang<sup>®</sup>, Senior Member, IEEE, and Thomas Weller<sup>®</sup>, Fellow, IEEE

Abstract—Suspended finite ground coplanar waveguide (FG-CPW) interconnects, fabricated with laser-enhanced direct print additive manufacturing (AM), are modeled and characterized in this work. The study focuses on the variation of characteristic impedance and attenuation with design geometry. Acrylonitrile butadiene styrene (ABS) is printed with fused deposition modeling (FDM) to form 10-mm-long suspended ABS bridges and Dupont CB028 is microdispensed to realize conductive traces on the ABS bridges. Femtosecond pulsed laser machining in the ultraviolet range is combined with the AM to create gaps ranging from 8 to 92 µm in width on either side of a signal line to define the FG-CPW. Three different suspended interconnects are designed, where the total linewidth (signal line plus gaps) is kept constant at 300  $\mu$ m for all designs, but the aspect ratio (AR) (signal linewidth divided by total linewidth) is varied. Two multiline thru-reflect-line calibrations are performed to measure each design: one uses printed calibration standards and the other employs a commercial calibration substrate. The attenuation of the interconnects at 30 GHz is 0.28, 0.13, and 0.06 dB/mm for ARs of 0.95, 0.87, and 0.38, respectively. The laser machining of the gaps results in partial substrate removal, which increases the characteristic impedance by approximately 11%. The impact of fabrication tolerances is examined.

Index Terms—3-D printing, additive manufacturing (AM), aspect ratio (AR), attenuation, characteristic impedance, femtosecond laser, finite ground coplanar waveguide (FG-CPW), machining, suspended interconnect, transmission line (TL).

### I. Introduction

WIRELESS communications hardware technologies are rapidly evolving due to the growing demand for higher

Manuscript received 27 March 2024; accepted 17 April 2024. Date of publication 13 May 2024; date of current version 28 June 2024. This work was supported in part by the U.S. National Science Foundation under Grant 1711790. Recommended for publication by Associate Editor K. Bock upon evaluation of reviewers' comments. (Corresponding author: Omer Faruk Firat.)

Omer Faruk Firat and Thomas Weller are with the School of Electrical Engineering and Computer Science, Oregon State University, Corvallis, OR 97331 USA (e-mail: firato@oregonstate.edu; tom.weller@oregonstate.edu).

Jing Wang is with the Department of Electrical Engineering, University of South Florida, Tampa, FL 33620 USA (e-mail: jingw@usf.edu).

Color versions of one or more figures in this article are available at https://doi.org/10.1109/TCPMT.2024.3399750.

Digital Object Identifier 10.1109/TCPMT.2024.3399750

data rates within compact and low-parasitic packaging. Nextgeneration wireless streaming and wireless high-definition multimedia interfaces require multigigabits per second data rates [1], [2]. Also, the Internet of Things (IoT) devices require ubiquitous connectivity between multiple devices in different environments. Millimeter-wave (mm-wave) wireless technologies can enable higher data rates with wide channel bandwidths at an operating frequency of tens to hundreds of gigahertz [3], [4]. However, as the frequency increases, the packaging and integration for wireless front-end components get more challenging due to increased loss and parasitic effects. System on package (SoP) is one of the technologies that can reduce interconnect loss and provide high-performance communication. This technique enables direct integration between integrated circuit (IC) dies and other active and passive components with planar and/or suspended interconnects [5], [6], [7].

Additive manufacturing (AM) is a flexible way to realize SoP by creating new packaging solutions for different types of IC dies and RF components [8], [9], [10], [11], [12], [13]. Minimizing the loss and controlling the characteristic impedance of the interconnects is especially important at mm-wave frequencies since wireless transceiver systems require well-controlled impedance and low loss. Oftentimes, the employment of AM eliminates the need for wire bonding and flip-chip bonding, which are the two most common integration techniques. Wire bonding is a relatively cost-effective and repeatable process, but at higher frequencies, it introduces detrimental parasitics and higher losses, thus worsening the frequency response of the system [14]. The flip-chip method reduces the parasitic effect by reducing the interconnection length, but it is sensitive to the coefficient of thermal expansion (CTE) mismatch between an IC chip, solder bumps, and interconnects [15]. AM suspended interconnects could be useful to realize the interconnection between electronics on a substrate and crossing over an IC, such as a low noise amplifier, embedded in a cavity [16], [17]. The contribution of this work is to explore mm-wave planar interconnects for SoP integration using AM.

Aerosol jet printing (AJP), inkjet printing (IJP), and microdispensing are the three prominent methods for

2156-3950 © 2024 IEEE. Personal use is permitted, but republication/redistribution requires IEEE permission. See https://www.ieee.org/publications/rights/index.html for more information.

depositing inks and pastes. AJP and IJP have the advantage of high print resolution compared to microdispensing. On the other hand, microdispensing can print more materials with a wider viscosity range from 1 to 10<sup>6</sup> cP and it can easily be integrated with fused deposition modeling (FDM). This technology enables the fabrication of 3-D structures with integrated electronics in a single automated platform, referred to as direct print AM (DPAM). It is possible to deposit thermoplastic and thermoplastic-ceramic composite materials with FDM [18], whereas conductive, resistive, and dielectric inks or pastes can be deposited with microdispensing [19]. Integrating a femto second laser to DPAM, referred to as laser-enhanced DPAM (LE-DPAM), mitigates conductor edge roughness effects and tapered line edges and leads to precise postprocessing ability to achieve down to 5  $\mu$ m of minimum feature size. Recent studies show that laser processing solidifies the conductive paste on the edges of a cutting path and creates a high conductivity region that significantly enhances the conductivity of treated conductors [20]. In addition to other AM works, LE-DPAM has been used to realize lumped passive elements [21], [22], RF MEMS switches [23], and low-loss packaging [24].

Coplanar waveguide (CPW) is a type of planar transmission line (TL), which consists of a center conductor and a pair of semi-finite ground planes on each side of the center conductor. CPW has been widely employed in RF systems because of its planar configuration and integration compatibility with monolithic microwave ICs (MMICs). However, ground planes can be a challenge for high-density integration due to their size, undesired parallel plate mode excitation, and radiation effects, especially for high-frequency applications. A finite ground coplanar waveguide (FG-CPW), where typically the ground planes hold approximately twice the width of the center conductor while being less than 1/8 of the wavelength, can mitigate both issues [25].

This article outlines the design, LE-DPAM fabrication, and characterization of suspended interconnects in the form of coplanar waveguides at microwave and mm-wave frequencies. A general design procedure for this TL geometry was first introduced in [23], where its use in a suspended RF switch structure was described. The contribution of this article is to detail the FG-CPW design procedure with a focus on the optimization of its performance with respect to geometry while considering the fabrication tolerances. This includes the study of femtosecond laser processing-induced fabrication tolerances and the variation of characteristic impedance and attenuation for three design geometries. A variation of  $+2 \mu m$ in gap dimensions and partial substrate removal at the bottom of the gaps increases the designed characteristic impedances by approximately 11%. The measured results show that the attenuation of the interconnects at 30 GHz varies from 0.06 to 0.28 dB/mm as the characteristic impedance decreases from approximately  $104-33 \Omega$ . To the best of the authors' knowledge, this is the first detailed demonstration of mm-wave, suspended TLs that are fabricated using an AM technique.

## II. DESIGN AND FABRICATION

Three suspended FG-CPW interconnects with aspect ratios (ARs) of 0.95, 0.87, and 0.38 are designed at 30 GHz using

TABLE I DESIGN MATRIX

Design	AR	W	g	L	Z <sub>0</sub> <sup>f</sup>	Z <sub>0</sub> <sup>n</sup>
		(µm)	(µm)	(mm)	$(\Omega)$	$(\Omega)$
1	0.95	284	8	10	30	33
2	0.87	260	20	10	44	49
3	0.38	116	92	10	93	104
Open	0.87	260	20	1	44	49
Thru	0.87	260	20	2	44	49
Delay 1	0.87	260	20	7.75	44	49
Delay 2	0.87	260	20	3.28	44	49
Delay 3	0.87	260	20	3.92	44	49

 $Z_0^{\rm f}$ = with flat substrate;  $Z_0^{\rm n}$ =with notched substrate. L is the line length. Finite ground width (FG<sub>w</sub>)=500 µm for all designs.

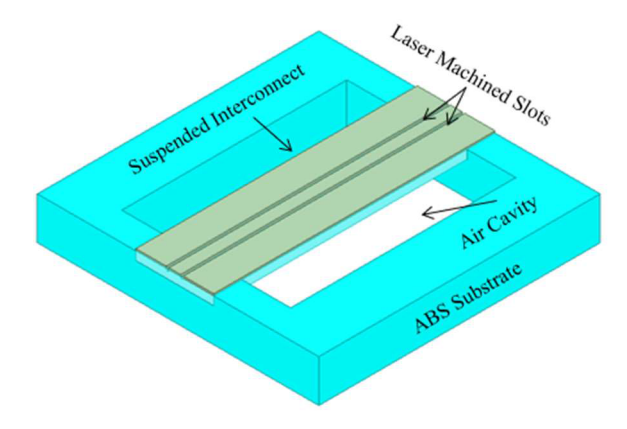


Fig. 1. Isometric view of the proposed suspended interconnect configuration.

advanced design system (ADS) Controlled Impedance Line Designer 2020 and Ansys HFSS 2021 R2, as illustrated in Figs. 1 and 2. The AR is calculated using (1), and the signal linewidth plus gaps (w+2 g) is kept constant at 300  $\mu$ m to properly demonstrate the impact of AR variation on characteristic impedance and attenuation. Fig. 3 demonstrates how AR influences attenuation across different frequencies. The design matrix is detailed in Table I with a finite ground width (FG<sub>w</sub>) and a conductor thickness (t) of 500 and 20  $\mu$ m, respectively, and a 400- $\mu$ m-thick substrate for the suspended bridges. In Table I,  $Z_0^f$  and  $Z_0^n$  refer to a line impedance that has a flat substrate and a notched substrate, respectively.  $Z_0^n$  values are higher than  $Z_0^f$  due to the notching from laser machining during the fabrication process, as detailed in this section

$$AR = \frac{w}{w + 2g}.$$
 (1)

Multiline thru–reflect–line printed calibration standards with an AR of 0.87 are used in this work. The characteristic impedance of the calibration standards with this AR becomes 49  $\Omega$  by taking the substrate notching into account. The open standard and thru standard lengths are 1 and 2 mm, respectively. The three delay lines are a quarter wavelength ( $\lambda/4$ ) longer than the thru standard at 10, 30, and 45 GHz. The wavelength is calculated at these three frequencies using

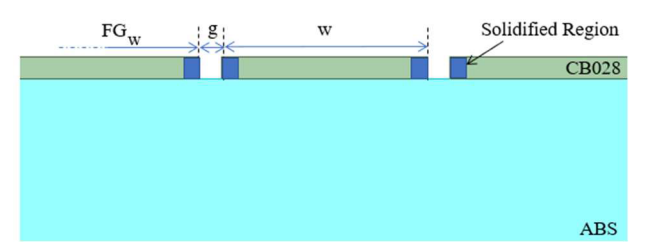


Fig. 2. Cross-sectional view of a laser-machined suspended interconnect with solidified high conductivity region.

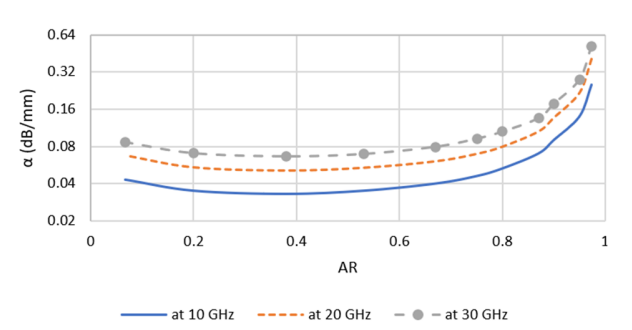


Fig. 3. Simulation of attenuation (dB/mm) versus AR at three frequencies. Simulations assume CPW lines as shown in Fig. 2 with a 300- $\mu$ m total linewidth (w+2 g).

effective permittivity ( $\varepsilon_{\rm eff}$ ) as seen in (2) and (3). The resulting total lengths of the delay lines are 7.75, 3.92, and 3.28 mm

$$\varepsilon_{\text{eff}} = \frac{(1 + \varepsilon_r)}{2} = 1.69 \tag{2}$$

where

$$\varepsilon_r = 2.38$$

$$\lambda = \frac{c}{f\sqrt{\varepsilon_{\text{eff}}}}$$

$$\frac{\lambda}{4} = 5.75 \text{ mm at } 10 \text{ GHz}$$

$$\frac{\lambda}{4} = 1.92 \text{ mm at } 30 \text{ GHz}$$
and 1.28 mm at 45 GHz.

A digital AM platform, nScrypt 3Dn tabletop 3-D printer integrated with a Clark MXR Impulse femtosecond laser as depicted in Fig. 4, was used to realize the 10-mm-long suspended FG-CPW lines along with the mTRL calibration standards. This AM platform combines FDM and microdispensing. Acrylonitrile butadiene styrene (ABS) with a dielectric constant  $(\varepsilon_r)$  of 2.38 and a loss tangent of 0.0065 measured at 30 GHz [26] was chosen as the filament-based thermoplastic to fabricate the substrate.

A flip print technique was developed to 3-D print well-controlled free-standing ABS bridges in a repeatable manner. This technique was used for the first time in our previous study [23] to enable the 3-D printing of suspended bridges of arbitrary dimensions without problems related to bending or warping. Extruding a 10-mm-long ABS bridge that is a few millimeters in width over a cavity is challenging because the bridge tends to sag and take the circular shape of the ceramic nozzle since there is no support underneath. Our previous study shows that after a length of 2 mm, the bridges start sagging in the middle [16]. Using the flip print strategy,

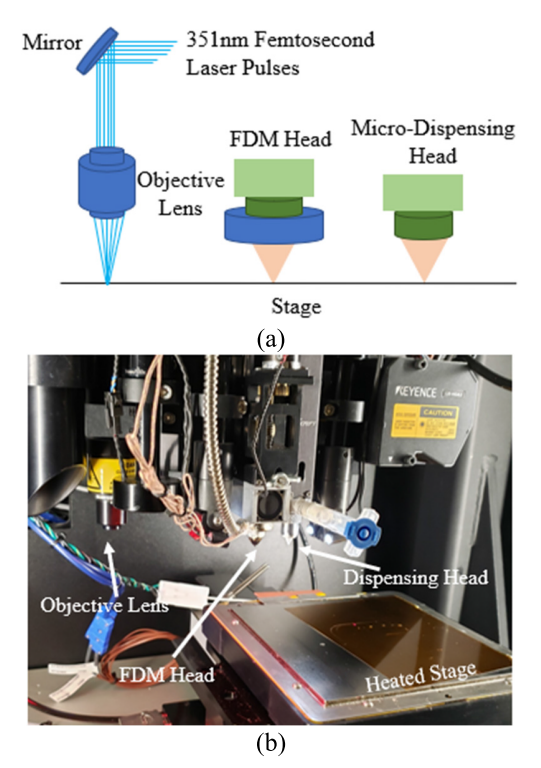


Fig. 4. (a) Cross-sectional view illustration of nScrypt 3Dn TableTop printer with a Clark MXR femtosecond UV laser and (b) photograph of the nScrypt 3Dn printer.

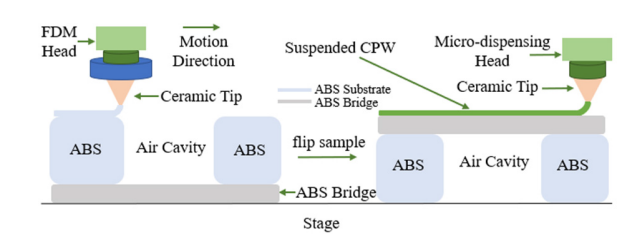


Fig. 5. Simplified DPAM fabrication process flow of the suspended FG-CPW line by FDM and microdispensing.

an ABS bridge is extruded as a first layer on the printer stage, and once the print process is completed, the sample is flipped, so the ABS bridge becomes the top layer. This process is illustrated in Fig. 5. This method offers custom design freedom in two dimensions and achieves ABS bridges with low surface roughness since they are directly extruded onto the print bed. In this way, ABS was extruded at 240 °C through a 125-\mu m inner/175-\mu m outer diameter ceramic nozzle onto a 110 °C heated print bed. The suspended regions were defined with two ABS supports, as shown in Fig. 5. The suspended nature of the lines used here is a consideration for the way they are fabricated, but due to the thickness of the substrate, it does not measurably impact the high-frequency electrical performance of the proposed FG-CPW lines.

Conductive silver paste (Dupont CB028) with an average thickness of 20  $\mu m$  was microdispensed with a 125- $\mu m$  inner/175- $\mu m$  outer diameter ceramic nozzle onto the ABS bridges. The silver paste was also dispensed on a nonsuspended ABS region to form the mTRL calibration standards. A curing process was performed to evaporate solvents in the

conductor paste at 90 °C for 1.5 h, after which the printed CB028 silver paste achieved a conductivity of 1.65e6 S/m.

The femtosecond pulsed laser operating at 351-nm wavelength and 200-kHz repetition rate was characterized and used to realize the FG-CPW lines by cutting a gap on either side of the center conductor. A typical line is shown in Fig. 6(a). To use the laser most effectively, a detailed study of laser power, machining speed, and a number of passes with a high-magnification objective lens  $(15\times)$  was performed. It was observed that 60-mm/s speed with an average power level (Pavg) of 60 mW is an optimum condition to achieve wellcontrolled geometry, namely, gap width and AR. While the laser creates the gaps, it also fuses together the silver flakes of the CB028 in a  $\sim 1.5 - \mu m$  region near the gap edges, as depicted in Figs. 2 and 6(d). These treated CB028 regions adjacent to the gaps increase the effective conductivity of the metallization layers significantly. A 3-D EM (Ansys Electronic Desktop) simulation was performed to extract the effective conductivity  $\sigma_{\rm eff}$  of the printed traces, which represents the net effect of having a region of high conductivity on the inner edges of the gaps (treated region) with the rest of the conductor layer having a lower conductivity (nontreated region). It was found that the  $\sigma_{\rm eff}$  value increases from 1.65e6 to 5e6 S/m with the treated regions. This conductivity value for CB028 is used in all simulations in this work.

The characteristics of the TLs change depending on the fabrication-related artifacts. In an ideal case, the substrate is fully intact, and ABS fills the lower half-space underneath the CB028. In a realistic scenario, however, there is some removal of ABS under the gaps because of the laser machining. This notching is seen in cross-sectional scanning electron microscope (SEM) images, see Fig. 6(g)-(i). The partial removal of ABS, referred to as cut depth (cut<sub>sub</sub>), gets deeper as the gap width increases. It is approximately 30, 110, and 170  $\mu$ m for Designs 1-3, respectively. The change in the depth of the cut is related to thermal behavior as the cutting distance gets farther from the thermally conductive CB028 silver paste. For these three designs, the notching increases the characteristic impedance by approximately 11% (see Table I) and is thus important to account for in the simulations. A second artifact to consider is the variation in gap width due to fabrication tolerances. As observed from the SEM images, this variation is approximately  $\pm 2 \mu m$  irrespective of the line dimensions. The impact of this artifact on attenuation and return loss is discussed in Section III.

# III. SIMULATION AND RESULTS

Ansys Electronic Desktop 2021 R2 was used to model the suspended FG-CPW lines. The measured cut<sub>sub</sub> values from SEM images for each design were considered for the simulations. Measurements were performed using a Keysight performance network analyzer (PNA) N55227A with GGB Industries ground signal ground (GSG) 200- $\mu$ m pitch size RF probes. Each FG-CPW line was measured using two separate calibrations for comparison purposes, one with printed mTRL standards and one using a 50- $\Omega$  CS-5 calibration substrate from GGB Industries. Cascade Wincal XE software was used to calculate the calibration coefficients.

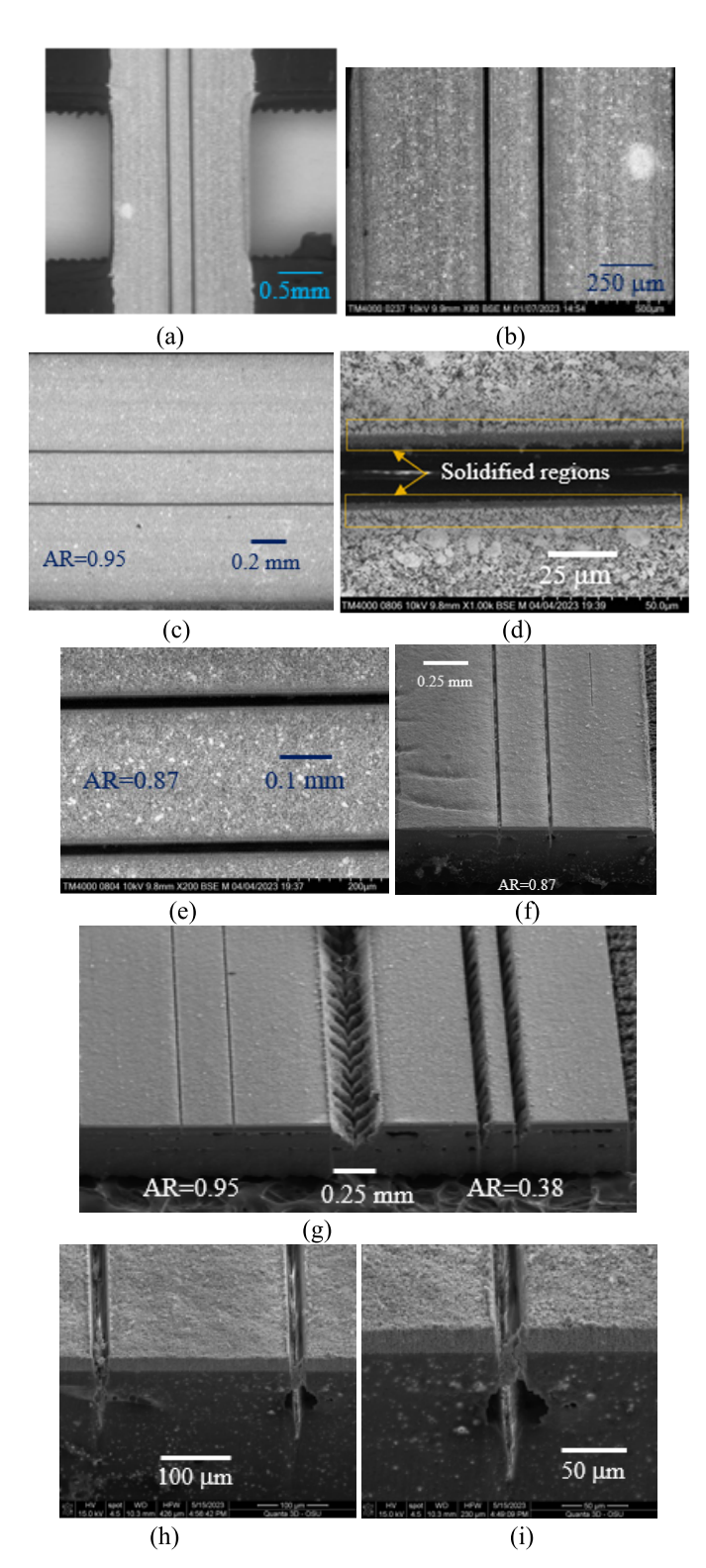


Fig. 6. SEM images of suspended interconnects including (a) CPW over a 2-mm-long cavity (a 10-mm-long line is difficult to capture in a photograph), (b)–(e) top view of signal lines with gaps at different magnifications, and (f)–(i) cross-sectional views of different AR CPW lines. The sample was cut to do cross-sectional imaging and this process left some particles on gaps.

The measured and simulated data are compared in Figs. 7–9. Two different samples (A and B) for each design were fabricated and measured to evaluate the repeatability of the fabrication process and the measurement results obtained

TABLE II
ATTENUATION COMPARISON AT 30 GHZ

AR	Simulation		Measurement				Mean	Standard Deviation
	(dB/1	mm)		(dB/mm)				
	No ABS	ABS	Printed	mTRL	CS-5			
	removal	removal	Sample		Sample			
			A	В	A	В		
0.95	0.29	0.28	0.28	0.29	0.27	0.3	0.285	0.008
0.87	0.14	0.13	0.13	0.13	0.13	0.14	0.136	0.004
0.38	0.07	0.05	0.06	0.06	0.06	0.06	0.062	0.0014

TABLE III
COMPARISON WITH OTHER WORKS

Ref.	$Z_0(\Omega)$	w	g	α (dB/mm)	Process
TEL:	33	284	8	0.35 at 40 GHz	LE-DPAM with 351 nm laser
This	49	260	20	0.16 at 40 GHz	LE-DPAM with 351 nm laser
work	104	116	92	0.08 at 40 GHz	LE-DPAM with 351 nm laser
[28]	50	29	15	0.7 at 40 GHz	AJP on Alumina CPW
[29]	70	160	50	0.23 at 40 GHz	AJP on Kapton CPW
[30]	50	NA	NA	0.5 at 60 GHz	Inkjet on LCP CPW
[9]	50	NA	NA	0.5 at 40 GHz	Inkjet on polymer CPW
[26]	50	300	20	0.36 at 40 GHz	LE-DPAM with 1064 nm

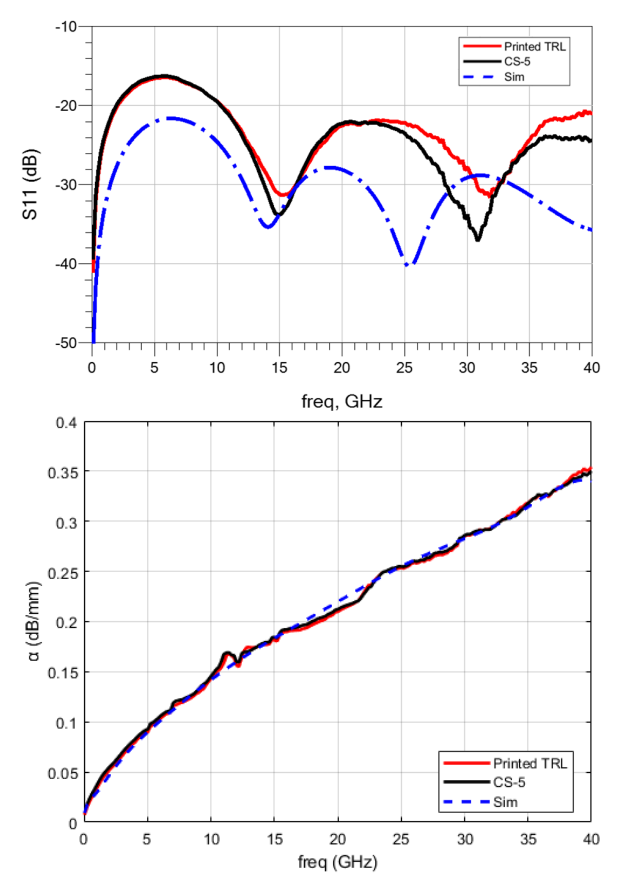
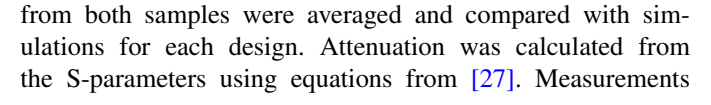


Fig. 7. Simulation versus measurement results for 10-mm-long suspended FG-CPW line with an AR of 0.95.



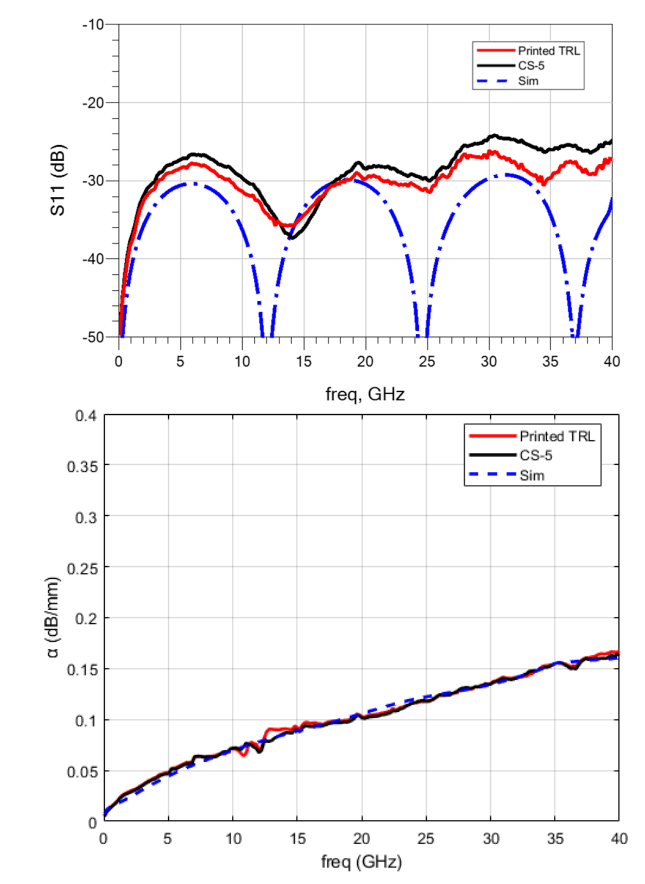


Fig. 8. Simulation versus measurement results for 10-mm-long suspended FG-CPW line with an AR of 0.87.

that used the calibration performed with printed standards are in close agreement with those obtained using the calibration performed with the GGB CS-5 substrate.

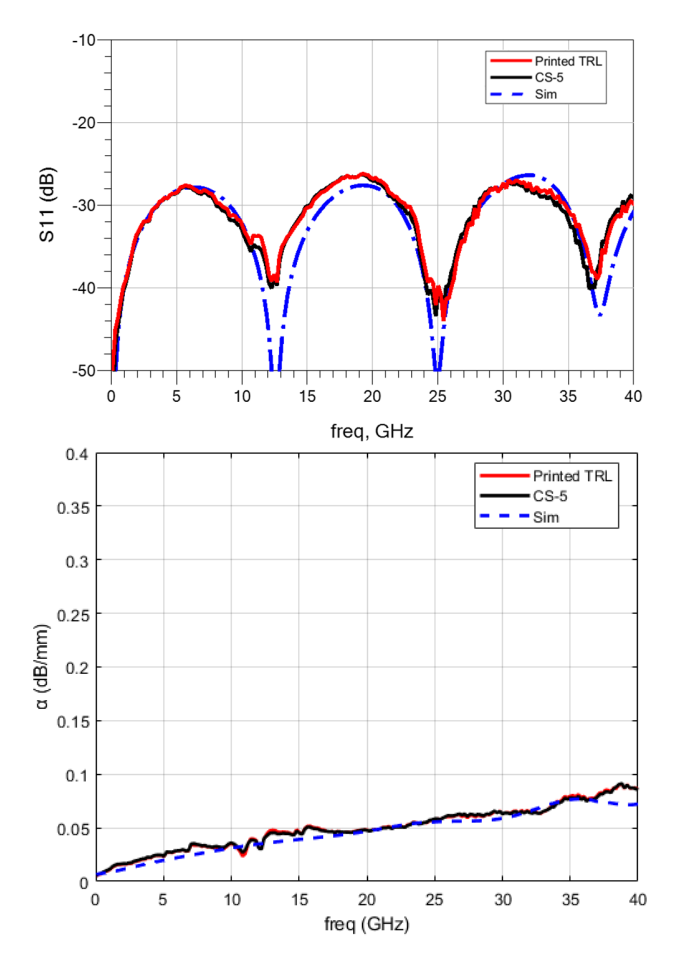


Fig. 9. Comparison of simulated and measured results for 10-mm-long suspended FG-CPW line with an AR of 0.38.

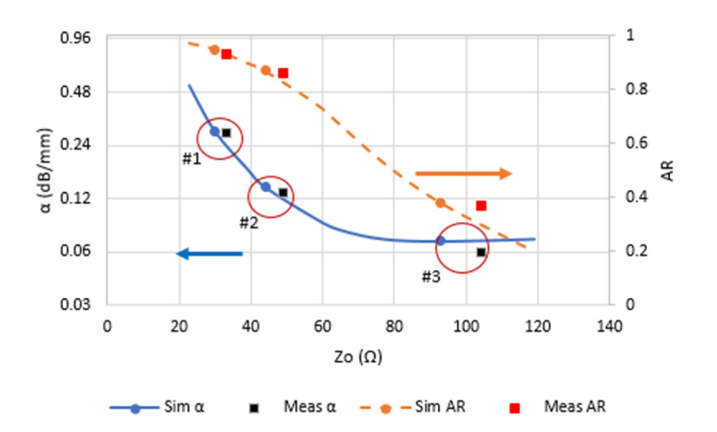


Fig. 10. Simulated and measured attenuation ( $\alpha$ ) and AR versus characteristic impedance ( $Z_0$ ) at 30 GHz. The simulation data, including simulated AR calculation, assume the ideal nonnotched FG-CPW lines, as shown in Fig. 2.

An analysis of the measured results and the geometry of the fabricated samples provides insights into the influence of the design attributes on the attenuation characteristics. Fig. 10 shows that the attenuation decreases as  $Z_0$  increases to around  $80~\Omega$ , and it then levels off. Correspondingly, the attenuation decreases as AR decreases. The attenuation is 0.28, 0.13, and 0.06 dB/mm at 30 GHz for AR of 0.95, 0.87, and 0.38, respectively. Table II presents attenuation variation at 30 GHz due to the fabrication tolerances for samples A and B. The

variation for Design 1 is larger compared to the other two designs due to the higher AR as shown in Fig. 3 that the attenuation of high AR designs is more sensitive to imperfections in geometry compared to that of low AR designs. Attenuation variation overall is still less than 0.05 dB/mm for the three designs at 30 GHz. The gap width tolerance also affects the characteristic impedance and, thus, the return loss. This may contribute to the discrepancies between the simulated and measured  $S_{11}$  data, which are most noticeable for the high AR design for which the change in  $Z_0$  is most sensitive to variations in geometry. However, these discrepancies do not measurably affect the extracted attenuation values since they generally occur when  $S_{11}$  is below -20 dB.

EM simulation-based analyses using HFSS were performed to determine the complex characteristic impedance of the lines  $(Z_0^n$  along with their frequency dependence and examine the impact on the extracted attenuation when the complex value is used as the reference impedance instead of a real-valued  $Z_0$ . This is carried out to confirm the accuracy of using a constant real value reference impedance during the mTRL calibration process. The complex characteristic impedances for Designs 1-3 are 33 - j1.2, 49 - j0.8, and 104 - j0.6  $\Omega$ at 30 GHz. Using 30-GHz data across all the designs, the imaginary part of  $Z_0^n$  is less than 3.5% of the corresponding real parts. To assess the impact of the complex impedance on the extracted attenuation, the simulated 30-GHz HFSS S-parameter responses were normalized to 50  $\Omega$  and subsequently renormalized to the complex value and real-part value of  $Z_0^n$ . From these two sets of data, the resulting difference in the attenuation constant (in Np/m) is less than 0.3%. The difference in the phase constant at 30 GHz across all designs, determined from simulations that assume either lossy or lossless materials, is less than 6%, which brings a slight shift on  $S_{11}$ . The simulation results also show that the real part of  $Z_0$  changes by less than 3.5% across all cases, with AR = 0.95 being the most frequency-dependent from 10 to 40 GHz, so it is assumed that  $Z_0$  is independent of frequency. Consequently, it is deemed to be sufficient to adopt only the constant real part of the characteristic impedance for the mTRL calibration of the measured data presented herein.

To demonstrate the performance achieved using LE-DPAM, a comparison with other additively manufactured TLs from the literature is presented. Table III compares different FG-CPW line attenuations, where  $Z_0$  represents the measured line impedance. In [28] and [29], planar CPWs fabricated with AJP have the signal linewidths of 29 and 160  $\mu$ m. In [26], a planar CPW is also realized with the method of LE-DPAM and has a signal width of 300  $\mu$ m. In [9] and [30], CPWs are printed on dielectric ramps with IJP. The lines realized by laser micromachining exhibit superior performance due to the enhanced conductivity achieved through laser machining.

# IV. CONCLUSION

This article has presented a thorough study on suspended FG-CPW interconnects that are fabricated using a laser-enhanced direct print AM (LE-DPAM) approach. These interconnects provide a possible solution for mm-wave SoP implementations, such as designs that require signal routing

across ICs embedded in cavities, and they could also be co-designed with a fluidics-based thermal management system for enhancing power handling capability. Using a flip-print process, interconnects up to 10 mm in length are fabricated across open cavities. The lines are 300  $\mu m$  wide, with ARs ranging from 0.95 to 0.38 and corresponding characteristic impedance varying from 33 to 104  $\Omega$ . The measured attenuation at 30 GHz varies from 0.28 to 0.06 dB/mm, exhibiting a decreasing trend with increasing characteristic impedance.

It is important to study the fundamentals of interconnects to achieve the desired minimum attenuation and power handling capability for advanced packaging systems at mm-wave frequencies [31]. In the fabricated structures, the gap width that is defined by the femtosecond laser machining varies by  $\pm 2 \mu m$ . Laser machining notches the substrate and this substrate removal gets deeper as the gap width increases. The notching depth ranges from 30 to 170  $\mu$ m for the corresponding gap width that changes from 8 to 96  $\mu$ m. For the lines tested herein, these laser machining tolerances resulted in less than 0.05-dB/mm variation in TL attenuation at 30 GHz, whereas an increase in resulting characteristic impedance of approximately 11% was observed that can be primarily ascribed to the notching of the substrate. The results of geometry provide insights into the influence of the design attributes on the attenuation characteristics.

### REFERENCES

- P. Wang, Y. Li, L. Song, and B. Vucetic, "Multi-gigabit millimeter wave wireless communications for 5G: From fixed access to cellular networks," *IEEE Commun. Mag.*, vol. 53, no. 1, pp. 168–178, Jan. 2015, doi: 10.1109/MCOM.2015.7010531.
- [2] Z. Ma, M. Xiao, Y. Xiao, Z. Pang, H. V. Poor, and B. Vucetic, "High-reliability and low-latency wireless communication for Internet of Things: Challenges, fundamentals, and enabling technologies," *IEEE Internet Things J.*, vol. 6, no. 5, pp. 7946–7970, Oct. 2019, doi: 10.1109/JIOT.2019.2907245.
- [3] S. K. Yong and C.-C. Chong, "An overview of multigigabit wireless through millimeter wave technology: Potentials and technical challenges," *EURASIP J. Wireless Commun. Netw.*, vol. 2007, no. 1, p. 50, Dec. 2006.
- [4] I. G. Smith, "The Internet of Things 2012 new horizons," in IERC European Research Cluster on the Internet of Things. Halifax, U.K.: Halifax, 2012.
- [5] K. K. Samanta and I. D. Robertson, "Surfing the millimeter-wave: Multilayer photoimageable technology for high performance SoP components in systems at millimeter-wave and beyond," *IEEE Microw. Mag.*, vol. 17, no. 1, pp. 22–39, Jan. 2016.
- [6] C. Mariotti, B. S. Cook, F. Alimenti, L. Roselli, and M. M. Tentzeris, "Additively manufactured multilayer high performance RF passive components on cellulose substrates for Internet-of-Things electronic circuits," in *IEEE MTT-S Int. Microw. Symp. Dig.*, May 2015, pp. 1–4.
- [7] M. T. Craton, J. D. Albrecht, P. Chahal, and J. Papapolymerou, "Additive manufacturing of a wideband capable W-band packaging strategy," *IEEE Microw. Wireless Compon. Lett.*, vol. 31, no. 6, pp. 697–700, Jun. 2021.
- [8] R. A. Ramirez, D. Lan, J. Wang, and T. M. Weller, "MMIC packaging and on-chip low-loss lateral interconnection using additive manufacturing and laser machining," in *IEEE MTT-S Int. Microw. Symp. Dig.*, Jun. 2017, pp. 38–40.
- [9] B. K. Tehrani, B. S. Cook, and M. M. Tentzeris, "Inkjet-printed 3D interconnects for millimeter-wave system-on-package solutions," in *IEEE MTT-S Int. Microw. Symp. Dig.*, San Francisco, CA, USA, May 2016, pp. 1–4, doi: 10.1109/MWSYM.2016.7540084.
- [10] O. F. Firat, R. Tipton, V. Bhethanabotla, J. Wang, and T. Weller, "Versatility of laser enhanced direct print additive manufacturing," in *Proc. NIP Digit. Fabr. Conf.*, Oct. 2021, no. 1, pp. 32–36.

- [11] R. Sorrentino and O. A. Peverini, "Additive manufacturing: A key enabling technology for next-generation microwave and millimeter-wave systems [point of view]," *Proc. IEEE*, vol. 104, no. 7, pp. 1362–1366, Jul. 2016, doi: 10.1109/JPROC.2016.2577327.
- [12] J. G. Hester et al., "Additively manufactured nanotechnology and origami-enabled flexible microwave electronics," *Proc. IEEE*, vol. 103, no. 4, pp. 583–606, Apr. 2015.
- [13] J. A. Byford, M. I. M. Ghazali, S. Karuppuswami, B. L. Wright, and P. Chahal, "Demonstration of RF and microwave passive circuits through 3-D printing and selective metalization," *IEEE Trans. Compon., Packag., Manuf. Technol.*, vol. 7, no. 3, pp. 463–471, Mar. 2017.
- [14] S. Beer et al., "Design and measurement of matched wire bond and flip chip interconnects for D-band system-in-package applications," in *IEEE MTT-S Int. Microw. Symp. Dig.*, Jun. 2011, pp. 1–4.
- [15] A. Jentzsch and W. Heinrich, "Theory and measurements of flip-chip interconnects for frequencies up to 100 GHz," *IEEE Trans. Microw. Theory Techn.*, vol. 49, no. 5, pp. 871–878, May 2001.
- [16] O. F. Firat, M. M. Abdin, J. Wang, and T. M. Weller, "Low-Loss suspended crossover interconnects using laser enhanced direct print additive manufacturing," in *Proc. IEEE 20th Wireless Microw. Technol. Conf. (WAMICON)*, Cocoa Beach, FL, USA, Apr. 2019, pp. 1–4, doi: 10.1109/WAMICON.2019.8765445.
- [17] R. Zhang, J. C. C. Lo, and S. W. R. Lee, "Design and fabrication of a silicon interposer with TSVs in cavities for three-dimensional IC packaging," *IEEE Trans. Device Mater. Rel.*, vol. 12, no. 2, pp. 189–193, Jun. 2012, doi: 10.1109/TDMR.2012.2190764.
- [18] V. Kosamiya and J. Wang, "High-k and low-loss dielectric composite feedstock filaments, tailored for additive manufacturing of microwave devices," in *IEEE MTT-S Int. Microw. Symp. Dig.*, Los Angeles, CA, USA, Aug. 2020, pp. 928–931, doi: 10.1109/IMS30576.2020.9223844.
- [19] O. F. Firat, J. Wang, and T. Weller, "Additively manufactured metal-insulator-metal capacitors using a high-K dielectric paste," in *Proc. IEEE Int. Symp. Antennas Propag. USNC-URSI Radio Sci. Meeting (AP-S/URSI)*, Denver, CO, USA, Jul. 2022, pp. 1596–1597, doi: 10.1109/AP-S/USNC-URSI47032.2022.9887281.
- [20] M. Kacar, T. Weller, and G. Mumcu, "Conductivity improvement of microdispensed microstrip lines and grounded coplanar waveguides using laser micromachining," *IEEE Trans. Compon., Packag., Manuf. Technol.*, vol. 10, no. 12, pp. 2129–2132, Dec. 2020, doi: 10.1109/TCPMT.2020.3038332.
- [21] O. Firat, J. Wang, and T. Weller, "Laser-assisted and additively manufactured multilayer metal-insulator-metal capacitors," in *Proc. IEEE 22nd Annu. Wireless Microw. Technol. Conf. (WAMICON)*, Clearwater, FL, USA, Apr. 2022, pp. 1–4, doi: 10.1109/WAMI-CON53991.2022.9786110.
- [22] R. A. Ramirez, E. A. Rojas-Nastrucci, and T. M. Weller, "Laser-assisted additive manufacturing of mm-wave lumped passive elements," *IEEE Trans. Microw. Theory Techn.*, vol. 66, no. 12, pp. 5462–5471, Dec. 2018, doi: 10.1109/TMTT.2018.2873294.
- [23] O. F. Firat, J. Wang, and T. M. Weller, "Additively manufactured, low loss 20 GHz DC contact RF MEMS switch using laterally actuated, fix-free beam," in *IEEE MTT-S Int. Microw. Symp. Dig.*, Atlanta, GA, USA, Jun. 2021, pp. 135–138, doi: 10.1109/IMS19712.2021.9574805.
- [24] E. A. Rojas-Nastrucci, R. Ramirez, D. Hawatmeh, D. Lan, J. Wang, and T. Weller, "Laser enhanced direct print additive manufacturing for mm-wave components and packaging," in *Proc. Int. Conf. Electromagn. Adv. Appl. (ICEAA)*, Sep. 2017, pp. 1531–1534.
- [25] G. E. Ponchak, E. M. Tentzeris, and L. P. Katehi, "Characterization of finite ground coplanar waveguide with narrow ground planes," *Int. J. Microcircuits Electron. Packag.*, vol. 20, pp. 167–173, Feb. 1997.
- [26] E. A. Rojas-Nastrucci et al., "Characterization and modeling of K-band coplanar waveguides digitally manufactured using pulsed picosecond laser machining of thick-film conductive paste," *IEEE Trans. Microw. Theory Techn.*, vol. 65, no. 9, pp. 3180–3187, Sep. 2017.
- [27] W. R. Eisenstadt and Y. Eo, "S-parameter-based IC interconnect transmission line characterization," *IEEE Trans. Compon.*, *Hybrids*, *Manuf. Technol.*, vol. 15, no. 4, pp. 483–490, Aug. 1992, doi: 10.1109/33.159877.
- [28] A. Delage et al., "Aerosol jet printing of millimeter wave transmission lines on 3D ceramic substrates made by additive manufacturing," in IEEE MTT-S Int. Microw. Symp. Dig., Jun. 2018, pp. 1557–1560.
- [29] M. Abt et al., "Aerosol-printed highly conductive Ag transmission lines for flexible electronic devices," *IEEE Trans. Compon., Packag., Manuf. Technol.*, vol. 8, no. 10, pp. 1838–1844, Oct. 2018, doi: 10.1109/TCPMT.2018.2869977.

- [30] B. K. Tehrani, R. A. Bahr, W. Su, B. S. Cook, and M. M. Tentzeris, "E-band characterization of 3D-printed dielectrics for fullyprinted millimeter-wave wireless system packaging," in *IEEE MTT-S Int. Microw. Symp. Dig.*, Jun. 2017, pp. 1756–1759, doi: 10.1109/MWSYM.2017.8058985.
- [31] W.-Y. Yin, Y. Zhang, X. Dong, and Y. B. Gan, "Average power-handling capability of the signal line in coplanar waveguides on polyimide and GaAs substrates including the irregular line edge shape effects," *Int. J. RF Microw. Comput.-Aided Eng.*, vol. 15, no. 2, pp. 156–163, Mar. 2005.



Omer Faruk Firat (Student Member, IEEE) received the B.S. degree in electrical and electronics engineering from İnönü University, Malatya, Turkey, in 2013, and the M.S. degree in electrical engineering from the University of Delaware, Newark, DE, USA, in 2017. He is currently pursuing the Ph.D. degree with Oregon State University, Corvallis, OR, USA.

His research interests include microwave circuit designs for system-on-package integration, mm-wave interconnects and their power handling

capabilities, RF MEMS switches, antennas, and bias networks using the method of laser-enhanced direct print additive manufacturing.



Jing Wang (Senior Member, IEEE) received the dual B.S. degree in mechanical engineering and electrical engineering from Tsinghua University, Beijing, China, in 1999, and the dual M.S. degree in electrical engineering and mechanical engineering and the Ph.D. degree from the University of Michigan, Ann Arbor, MI, USA, in 2002 and 2006, respectively.

He is currently a Professor with the Department of Electrical Engineering, University of South Florida, Tampa, FL, USA. His research work has been

funded by federal agencies [National Science Foundation (NSF), Defense Threat Reduction Agency (DTRA), U.S. Army, and U.S. Air Force] and many companies totaling over \$16 M. He has authored or coauthored more than 180 peer-reviewed articles and holds 11 U.S. patents. His current research interests include RF additive manufacturing for structural electronics and packaging, RF/microwave/millimeter-wave circuits, phased antennas, and systems, monolithic microwave integrated circuits (MMICs), micromachined transducers, RF/bio-MEMS, wireless sensors, and functional nanomaterials.

Dr. Wang was a recipient of the 2018 Faculty Outstanding Research Achievement Award at the University of South Florida.



**Thomas Weller** (Fellow, IEEE) received the B.S., M.S., and Ph.D. degrees in electrical engineering from the University of Michigan, Ann Arbor, MI, USA, in 1988, 1991, and 1995, respectively.

From 1988 to 1990, he was at Hughes Aircraft Company, El Segundo, CA, USA. From 1995 to 2018, he was a Faculty Member at the University of South Florida, Tampa, FL, USA. In 2018, he joined Oregon State University, Corvallis, OR, USA, where he is currently the Michael and Judith Gaulke Professor and the Head

of the School of Electrical Engineering and Computer Science. In 2001, he co-founded Modelithics, Inc. His research interests include tunable and reconfigurable microwave circuits, microwave applications of additive manufacturing and 3-D printing, electromagnetic sensors, passive microwave circuit design, planar and 3-D electrically small antennas, and equivalent circuit modeling.